Code dependencies of pre-supernova evolution and nucleosynthesis in massive stars: evolution to the end of core helium burning

S. Jones,[1,2]★† R. Hirschi,[2,3]† M. Pignatari,[4]† A. Heger,[5,6,7]† C. Georgy,[2] N. Nishimura,[2] C. Fryer[8] and F. Herwig[1,7]†

[1]*Department of Physics and Astronomy, University of Victoria, Victoria, BC V8W 3P6, Canada*
[2]*Astrophysics Group, Lennard Jones Building, Keele University, Staffordshire ST5 5BG, UK*
[3]*Kavli Institute for the Physics and Mathematics of the Universe (WPI), The University of Tokyo, Kashiwa, Chiba 277-8583, Japan*
[4]*Department of Physics, University of Basel, Klingelbergstrasse 82, CH-4056 Basel, Switzerland*
[5]*Monash Centre for Astrophysics, School of Mathematical Sciences, Building 28, M401, Monash University, Vic 3800, Australia*
[6]*Minnesota Institute for Astrophysics, School of Physics and Astronomy, University of Minnesota, Minneapolis, MN 55455, USA*
[7]*Joint Institute for Nuclear Astrophysics, University of Notre Dame, Notre Dame, IN 46556, USA*
[8]*Computational Physics and Methods (CCS-2), LANL, Los Alamos, NM 87545, USA*

ABSTRACT

Massive stars are key sources of radiative, kinetic and chemical feedback in the Universe. Grids of massive star models computed by different groups each using their own codes, input physics choices and numerical approximations, however, lead to inconsistent results for the same stars. We use three of these 1D codes – GENEC, KEPLER and MESA – to compute non-rotating stellar models of 15, 20 and 25 $M_\odot$ and compare their nucleosynthesis. We follow the evolution from the main sequence until the end of core helium burning. The GENEC and KEPLER models hold physics assumptions used in large grids of published models. The MESA code was set up to use convective core overshooting such that the CO core masses are consistent with those obtained by GENEC. For all models, full nucleosynthesis is computed using the NuGrid post-processing tool MPPNP. We find that the surface abundances predicted by the models are in reasonable agreement. In the helium core, the standard deviation of the elemental overproduction factors for Fe to Mo is less than 30 per cent – smaller than the impact of the present nuclear physics uncertainties. For our three initial masses, the three stellar evolution codes yield consistent results. Differences in key properties of the models, e.g. helium and CO core masses and the time spent as a red supergiant, are traced back to the treatment of convection and, to a lesser extent, mass loss. The mixing processes in stars remain the key uncertainty in stellar modelling. Better constrained prescriptions are thus necessary to improve the predictive power of stellar evolution models.

Key words: stars: abundances – stars: evolution – stars: interiors – stars: massive – supernovae: general – galaxies: abundances.

1 INTRODUCTION

Over the last few decades, several groups have calculated and published large grids of models across the massive star mass range and spanning several initial metallicities. Such grids of models have proved invaluable for those wishing to simulate, for example, core-collapse supernovae (e.g. O'Connor & Ott 2011; Müller, Janka & Marek 2012; Ugliano et al. 2012; Couch & Ott 2013; Nakamura et al. 2014), galactic chemical evolution (e.g. Chiappini, Matteucci & Gratton 1997; Kawata & Gibson 2003; Cescutti & Chiappini 2014) or population synthesis (e.g. Bruzual & Charlot 2003;

Eldridge & Stanway 2009). They are also important resources with which observations of directly imaged supernova progenitors can be compared (e.g. Smartt 2009; Fraser et al. 2011; Maund et al. 2011). It is difficult to quantify the uncertainties in predictive simulations or in determining the nature of an observation when the uncertainties in the underlying stellar evolution and nucleosynthesis models are themselves rather elusive. For such studies, it would be advantageous if one was able to know a priori some of the qualitative and quantitative differences that a simulation using the results of stellar modelling would exhibit had the stellar models been computing using different assumptions or indeed with a different stellar evolution code.

Massive stars are those which produce an inert iron core and, ultimately, explode as core-collapse supernovae (see, for a review,

Woosley, Heger & Weaver 2002). At solar metallicity, massive stars are those with initial masses greater than about 8–10 M$_\odot$, just below which super-asymptotic giant branch (AGB) stars and the progenitors of electron-capture supernovae are formed (Nomoto 1984; Eldridge & Tout 2004; Poelarends et al. 2008; Jones et al. 2013). Above initial masses of roughly 25 M$_\odot$ massive stars forming inert iron cores may end their lives as weak or failed supernovae in which black holes are formed (Heger et al. 2003). Dim, weakly energetic and failed supernovae, however, are likely the result of more complicated details of the stellar evolution than simply the initial mass of the star (O'Connor & Ott 2011; Ugliano et al. 2012). Those more massive still (around 120 M$_\odot$ and higher) can become unstable due to electron–positron pair creation before the star can develop an iron core (e.g. Heger & Woosley 2002; Heger et al. 2003; Yusof et al. 2013). These stars will likely not leave behind a compact remnant at all. In this study, we focus on the main massive star range studied, between 15 and 25 M$_\odot$.

Martins & Palacios (2013) have recently compared the observable properties predicted by massive star models computed with the Modules for Experiments in Stellar Astrophysics (MESA), STAREVOL, Geneva Stellar Evolution Code (GENEC), STERN, PADOVA, FRANEC codes to Galactic observations. Their study show that the post-main-sequence (MS) evolution differs significantly between the different codes but it is hard to analyse the differences when so many input physics are different between the different stellar evolution codes. In this study, by using a post-processing method for the full nucleosynthesis, we eliminate differences that could have arisen from different codes using different rates. Thus, this study focuses on a few key 'stellar' (mainly the treatment of convection) and 'numerical' ingredients of the models. For this reason, we also do not consider the effects of rotation in this study.

Massive stars are the primary producers of ^{16}O in the universe, along with most of the α elements (e.g. Mg, Si, Ca and Ti) and a significant fraction of the Fe-group elements (Kobayashi, Karakas & Umeda 2011). Therefore, galactic chemical evolution (GCE) simulations need to rely on robust predictions for massive stars, over a large range of stellar masses and initial metallicities. Massive stars are also the host of the weak s-process, responsible for the majority of the s-process abundances with $60 < A < 90$ in the Solar system (e.g. Raiteri et al. 1993; The, El Eid & Meyer 2007). This includes most of the solar Cu, Ga and Ge (Pignatari et al. 2010). Tur, Heger & Austin (2007, 2009) and West, Heger & Austin (2013) have investigated the sensitivity of weak s-process production in massive stars to both the triple-α (3α) and ^{12}C(α, γ)^{16}O reaction rates. The impact of the ^{12}C(α, γ)^{16}O was also considered in a number of different works, showing sometimes different results (see e.g. Imbriani et al. 2001; El Eid, Meyer & The 2004). The uncertainties in these reaction rates, which are important during helium and carbon burning, were shown by Tur et al. to induce large changes in the remnant (protoneutron star) masses, which propagate to the final (explosive) nucleosynthesis yields of massive stars. Uncertainties in the ^{12}C + ^{12}C reaction rate also propagate through into uncertainties in weak s-process element production, primarily via the impact that enhancing or reducing the rate has on the stellar structure during carbon burning (Gasques et al. 2007; Bennett et al. 2012; Pignatari et al. 2013a).

The aim of this work is to examine the structural differences in the evolution of massive stars as predicted by different published and unpublished stellar evolution models. In addition, we study the impact of these structural differences on the nucleosynthesis processes of 15, 20 and 25 M$_\odot$ stars. The NuGrid tools enable us to compare the nucleosynthesis in these stellar models using the same

set of reaction rates in a post-processing mode, drawing the focus of the comparison to differences in the structural evolution of the models and their impact on the nucleosynthesis. There are several well-established codes able to compute the evolution of massive stars: (in no particular order) GENEC, KEPLER, STERN (Brott et al. 2011), STARS (Eldridge & Tout 2004), FRANEC (Limongi & Chieffi 2012), TYCHO (Young & Arnett 2005) and MESA to name but a few. In this work, we limited ourselves to using the GENEC, KEPLER and MESA codes (see Section 2 for detailed descriptions of these codes) as a representative sample in order to be able to compare codes in greater detail.

This paper is structured as follows. In Section 2 we describe in detail the physics assumptions and numerical implementations of the codes. In Section 3 the structural evolution of the stellar models from the pre-MS is described, compared and contrasted. The nucleosynthesis calculations are presented in Section 4 and in Section 5 we summarize our results and discuss their implications in a broader context.

2 METHODOLOGY AND INPUT PHYSICS

Massive star models with initial masses of 15, 20 and 25 M$_\odot$ and initial metallicity $Z = 0.02$ were computed using three different stellar evolution codes. The calculations were performed using GENEC (see Eggenberger et al. 2008; Ekström et al. 2012), KEPLER (Weaver, Zimmerman & Woosley 1978; Rauscher et al. 2002; Woosley & Heger 2007, and citations therein) and MESA (Paxton et al. 2011, 2013), revision 3709. Concerning the models computed for this study, note that we do not expect any major changes between using this revision of MESA or later revisions including updates as described in Paxton et al. (2013). Baseline stellar physics assumptions are made, and feedback from rotation and magnetic fields is not considered as explained in the Introduction. In this section, we give a brief description of the codes and list the main input physics and assumptions.

The goal is not to obtain the same answer with all three codes. Rather, we aim to discuss the qualitative and quantitative differences between results from the three codes using standard choices for input physics for the GENEC and KEPLER codes, which have been adopted in most of their respective published models. Thus, we have focused on the most-studied massive star mass range (15–25 M$_\odot$). The input physics choices for MESA are explained presently in this section. We hope that this study will encourage the community to be vigilant when using grids of stellar evolution models (and yields) published by the different groups and to be better able to relate the differences in models to either the different choices made for input physics or the different design of the stellar evolution codes.

2.1 Code background

GENEC is a long-standing code that is most actively used to compute the structure and evolution of massive and solar-type stars. In its latest developments, it includes prescriptions for both rotation and magnetic fields (Eggenberger et al. 2008; Ekström et al. 2012). In GENEC, the equations of stellar structure, nuclear burning and mixing are solved in a decoupled manner. The structure equations are solved by means of a relaxation method that is usually referred to as the Henyey method (Henyey, Forbes & Gould 1964). In this time-implicit method first the structure equations, followed by the nuclear burning and finally the mixing are calculated in turn in an iterative scheme until the desired precision is reached.

Table 1. Overview of the mixing assumptions and operator coupling in the three stellar evolution codes (MESA, GENEC and KEPLER) that were used in this work. All three codes include prescriptions for rotation and magnetic fields, however, these physics were not included in the present study.

	MESA	GENEC	KEPLER
Operator coupling	Fully coupled (structure+burn+mix)	Decoupled (structure, burn, mix)	Partially coupled (structure+burn, mix)
Mixing strategy	Schwarzschild criterion with exponential–diffusive convective boundary mixing	Schwarzschild criterion with penetrative overshooting	Ledoux criterion with fast semiconvection
Implementation of mixing	Diffusion approximation	Instantaneous up to oxygen burning, then diffusion approximation	Diffusion approximation

The very external layers of the star – the 2 per cent of the total mass below the surface in non-rotating models – are not computed in the same way as the interior in GENEC. These external layers are solved using the pressure as the independent variable instead of the mass coordinate, allowing for a better discretization of the equations. Moreover, partial ionization is accounted for in the equation of state (EOS). For these external layers, GENEC assumes safely that there is no energy generation from nuclear burning.

The MESA (Paxton et al. 2011, 2013) program MESA/STAR is designed to solve the equations of stellar structure in a fully coupled manner. It is important to note that in MESA, different studies may use different choices for input physics (e.g. either the Ledoux or Schwarzschild criterion for convective stability) and there is not a single *recommended* set of input physics, although a time-dependent exponentially decaying diffusion scheme is typically used for convective boundary mixing. For this study, as described below, we chose input physics parameters for MESA that are as similar as possible to those in GENEC (e.g. mass-loss prescriptions) and we chose a convective boundary mixing f parameter that produces a CO core mass close to the CO core mass obtained with the GENEC and KEPLER codes. Thus, the MESA models represent something that a typical user could readily reproduce without the need to modify the code.

Finally, KEPLER is a spherical symmetric implicit hydrodynamic code (Weaver et al. 1978) tuned to problems in stellar evolution, with particular emphasis on proper modelling of the advanced stellar evolution stages until onset of core collapse; the evolution is stopped well before neutrino trapping starts to become important. Nuclear burning is implicitly coupled to the structure and full energy conservation is assured. Mixing is decoupled and treated in operator split, however, time-dependent mixing in diffusion approximation is used throughout. Extended nuclear burning is followed separately in coprocessing from the zero-age main sequences (ZAMS) to pre-supernova using an adaptive nuclear reaction network that automatically adds and removes isotopes as needed (Rauscher et al. 2002). KEPLER also includes rotation (Heger, Langer & Woosley 2000) and transport processes due magnetic fields (Spruit 2002; Heger, Woosley & Spruit 2005) but these are not used in the present study. KEPLER is able to model both hydrodynamic evolution phases and the supernova explosion (in a parametric way; Rauscher et al. 2002).

2.2 Input physics

There are numerous differences in the input physics assumptions made by the three stellar evolution codes that were used in this work. It is critical when comparing the results produced with

different codes to begin with a good understanding of their fundamental differences. To that end, in this section we list, compare and contrast the input physics assumptions made concerning the initial composition, opacities, nuclear reaction networks, nuclear reaction rates, mass-loss prescriptions, EOS, convection and overshooting and, finally, the initial models and treatment of the pre-MS. In Table 1 an overview of the mixing assumptions and operator coupling implementations in the three stellar evolution codes—which are two of the defining characteristics of the codes—is given.

2.2.1 Initial composition

The initial elemental abundances are scaled to $Z = 0.02$ from the solar distribution given by Grevesse & Noels (1993)[1] and the isotopic percentage for each element is given by Lodders (2003).

2.2.2 Opacities

The initial composition corresponds directly to the OPAL Type 2 opacity tables (Iglesias & Rogers 1996) used in GENEC, MESA and KEPLER (see below) for the present work. The electron conduction opacities used in GENEC are taken from Iben (1975). For lower temperatures in MESA and GENEC, the corresponding opacities from Ferguson et al. (2005) are used. The MESA opacity tables are in fact constructed from several sources, including the equations of Buchler & Yueh (1976) for $\log_{10}(T/K) > 8.7$ where Compton scattering becomes the dominant source of radiative opacity. For further details of the MESA opacity tables outside of the regions discussed here, we refer the reader to Paxton et al. (2011). The opacities used in KEPLER are the same as in Rauscher et al. (2002) and Woosley & Heger (2007): for temperatures below 10^9 K a set of opacities also described in Heger (1998) is used, with low-temperature opacity tables from Alexander & Ferguson (1994), opacity tables from Iglesias & Rogers (1996) at higher temperatures and for high temperatures and enriched compositions the Los Alamos Opacity tables (Huebener et al. 1964) and electron conduction are included. At higher temperature the opacities as described in Weaver et al. (1978) are used, including Iben (1975), Christy (1966), Cooper (1973), Chin (1965), Sampson (1959), Hubbard & Lampe (1969), Canuto (1970) where applicable and where outside the tables above.

---

[1] We acknowledge the measurements by Grevesse & Noels (1993) have since been succeeded by Asplund et al. (2009), however, this will not change dramatically any of the results of this code comparison study.

Table 2. Isotopes included in the nuclear reaction network of the various codes used in this paper.

	MESA	GENEC	KEPLER[a]
	A	A	A
n	1		1
p[b]			1
H	1, 2	1	1
He	3, 4	3, 4	3, 4
Li	7		
Be	7		
B	8		
C	12, 13	12, 13,	12
N	13–15	14, 15	14
O	15–21	16, 17, 18	16
F	17–23		
Ne	18–25	20, 21, 22	20
Na	20–27		
Mg	22–30	24, 25, 26	24
Al	24–31		
Si	27–32	28	28
P	30–34		
S	31–36	32	32
Cl	33–38		
Ar	35–40	36	36
K	37–42		
Ca	39–44	40	40
Sc	41–46		
Ti	43–50	44	44
V	45–52		
Cr	47–56	48	48
Mn	49–58		
Fe	51–60	52	52, 54
Co	53–62		
Ni	55–62	56	56

[a]APPROX-19 network.
[b]Protons from photodisintegration treated separately from ^{1}H in KEPLER for network stability.

2.2.3 Nuclear reaction network and reaction rates

The nuclear reaction network is an essential supplement to the structure equations, the EOS and the opacities. Because stellar evolution is so complex, it is costly to make a detailed evaluation of the nuclear composition for the entire star while solving the equations of stellar structure. Despite this, full yields from the stellar nucleosynthesis are highly desirable for galactic chemical evolution to test our understanding of the production sites of the heavy elements with $A \gtrsim 60$. In MESA, we use a network of 171 nuclear species (detailed in Table 2). GENEC includes the main reactions for hydrogen- and helium-burning phases and an α-chain type network for the advanced burning phases (even if it is now possible to extend it to a wide range of nuclear species and isotopes; Frischknecht, Hirschi & Thielemann 2012). The isotopes included explicitly in the network are listed in Table 2. Note that additional isotopes are included implicitly to follow the pp chains, CNO tricycles and $(\alpha, p)(p, \gamma)$ reactions in the advanced stages. In KEPLER, the APPROX-19 network follows a very similar approach, based on an α-chain network with light isotopes added and including additional reactions implicitly, e.g. for the CNO cycle and conversion of ^{22}Ne to ^{24}Mg. This network is used for energy generation and is implicitly coupled to structure, ensuring energy conservation. KEPLER can also follow an extended adaptive nuclear reaction network (BURN) in coprocess-

ing (see Rauscher et al. 2002; Woosley & Heger 2007, and references therein) or fully coupled (Woosley et al. 2004), replacing the APPROX-19 network. For the present work we have used the first approach (APPROX-19 combined with BURN in coprocessing) to have results more consistent with the other codes.

In GENEC, most reaction rates were taken from the NACRE (Angulo et al. 1999) reaction rate compilation for the experimental rates and from their website[2] for theoretical rates, while in MESA, preference was given to the REACLIB compilation (Cyburt et al. 2010). This includes several rates from the NACRE compilation fitted with the standard REACLIB fitting coefficients, for example for the ^{22}Ne$(\alpha, n)^{25}$Mg reaction. In KEPLER, reaction rates generally are from Rauscher & Thielemann (2000), supplemented by rates from Caughlan & Fowler (1988) and Rauscher et al. (2002). There are a few exceptions concerning the key energy-producing reactions. In GENEC, the rate of Mukhamedzhanov et al. (2003) was used for ^{14}N$(p,\gamma)^{15}$O below 0.1 GK and the lower limit NACRE rate was used for temperatures above 0.1 GK. This combined rate is very similar to the more recent LUNA rate (Imbriani et al. 2004) at relevant temperatures, which is used in MESA. In MESA and GENEC the Fynbo et al. (2005) rate was used for the 3α reaction and the Kunz et al. (2002) rate for ^{12}C$(\alpha, \gamma)^{16}$O. The ^{12}C + ^{12}C and ^{16}O + ^{16}O reaction rates were those of Caughlan & Fowler (1988). In KEPLER we use the ^{12}C$(\alpha, \gamma)^{16}$O rate of Buchmann (1996, 1997) multiplied by a factor 1.2 as suggested by West et al. (2013), and the rate of Caughlan & Fowler (1988) for 3α. In GENEC, the ^{22}Ne$(\alpha, n)^{25}$Mg rate was taken from Jaeger et al. (2001) and used for $T \le 1$ GK. The NACRE rate was used for higher temperatures. The ^{22}Ne$(\alpha, n)^{25}$Mg rate competes with ^{22}Ne$(\alpha, \gamma)^{26}$Mg, where the NACRE rate was used. The ^{22}Ne$(\alpha, n)^{25}$Mg rate from NACRE (Angulo et al. 1999) was used in the MESA code.

2.2.4 Mass loss

Several mass-loss rates are used depending on the effective temperature, $T_{\rm eff}$, and the evolutionary stage of the star in GENEC. For MS massive stars, where $\log T_{\rm eff} > 3.9$, mass-loss rates are taken from Vink, de Koter & Lamers (2001). Otherwise the rates are taken from de Jager, Nieuwenhuijzen & van der Hucht (1988). One exception is the $15\,M_\odot$ model, for which the mass-loss rates of de Jager et al. (1988) are used for the full evolution. For lower temperatures ($\log T_{\rm eff} < 3.7$), however, a scaling law of the form

$$\dot{M} = -1.479 \times 10^{-14} \times \left(\frac{L}{L_\odot} \right)^{1.7} \tag{1}$$

is used, where $\dot{M}$ is the mass-loss rate in solar masses per year, L is the total luminosity and $L_\odot$ is the solar luminosity (see Ekström et al. 2012, and references therein). In MESA, we adopt several mass-loss rates according to the scheme used in Glebbeek et al. (2009, wind scheme DUTCH in the code). For effective temperatures of $\log T_{\rm eff} < 4$ it uses mass-loss rates according to de Jager et al. (1988). For $\log T_{\rm eff} > 4$ there are two prescriptions that can be used, depending on the abundance of hydrogen at the surface. For $X_{\rm S}(^1$H$) > 0.4$ – a criterion satisfied by all of the models in this study throughout their entire evolution – the rates of Vink et al. (2001) are used. For the mass range considered in this paper (15–25 $M_\odot$), the mass-loss prescription used in KEPLER is from Nieuwenhuijzen & de Jager (1990); see Woosley & Heger (2007) for more details.

2.2.5 Equation of state

The EOS used in GENEC is that of a mixture of an ideal gas and radiation with pressure and temperature as the independent variables, and accounts for partial degeneracy in the interior during the advanced stages (see Schaller et al. 1992). In MESA, the EOS is in tabular form and is constructed from OPAL (Rogers & Nayfonov 2002) tables and for lower temperatures, the SCVH (Saumon, Chabrier & van Horn 1995) tables. For intermediate conditions, these two tables are blended in a pre-processing manner. Outside of the regions covered by these tables in the density–temperature plane, the HELM (Timmes & Swesty 2000) and PC (Potekhin & Chabrier 2010) equations of state are employed, again being blended at the boundaries of the tables. The EOS used in KEPLER is very similar to the one used in MESA. It is based on the work of Blinnikov, Dunina-Barkovskaya & Nadyozhin (1996, 1998) and has been compared to HELM by Timmes & Swesty (2000).

2.2.6 Convection and overshooting

In GENEC, convective stability is determined on the basis of the Schwarzschild criterion. Convective mixing is treated as instantaneous from hydrogen burning up to neon burning, where the composition across a convection zone is mass-averaged. The temperature gradient in the convective zones of the deep interior is assumed to be the adiabatic one, i.e. $\nabla = \nabla_{\rm ad}$, which is good to about one part in a million. The treatment of the external convective zones is made according to the mixing length theory with a mixing length parameter $\alpha_{\rm MLT} = 1.6$, and accounts for the non-adiabaticity of the convection for cool stars. Overshooting is only included for hydrogen- and helium-burning cores, where an overshooting parameter of $\alpha_{\rm OV} = 0.2H_P$ is used as in previous grids of non-rotating models (Schaller et al. 1992). The overshooting is implemented as an extension of the convective core by $\alpha_{\rm OV}$ above the strict Schwarzschild boundary and the overshooting region is considered to be part of the convective zone. Thus, the overshoot region is always chemically homogenized with the convective core.

Convection in MESA is treated at all times as a diffusive process, employing the assumptions of mixing length theory throughout the star with mixing length parameter $\alpha_{\rm MLT} = 1.6$, for which the diffusion coefficient is reduced exponentially at the boundary between convective and radiative layers as a function of radius (Freytag, Ludwig & Steffen 1996; Herwig et al. 1997),

$$D = D_0 \exp\left(-\frac{2z}{f_{\rm CBM}H_{P,0}}\right). \tag{2}$$

D is the diffusion coefficient as a function of distance z from the boundary location and $f_{\rm CBM}$ is a free parameter, for which we assume the value of 0.022 above and below all convective zones except for below convective shells in which nuclear burning is taking place, where we use $f_{\rm CBM} = 0.005$. D_0 is the diffusion coefficient, taken equal to the mixing length diffusion coefficient value ($D_{\rm MLT}$) at a distance $f_{\rm CBM}H_{P,S}$ inside the convection zone from the Schwarzschild boundary. At this location inside the convection zone, the pressure scale height is $H_{P,0}$, while $H_{P,S}$ is the pressure scale height at the Schwarzschild boundary. This is because the value of D_0 drops sharply towards zero at the Schwarzschild boundary. This treatment of convective boundary mixing is held from the MS until the end of core He burning.

KEPLER uses the Ledoux criterion for convection with an efficient semiconvection and a small amount of overshooting at the boundaries of convective regions to ensure numerical stability. KEPLER does not, however, use the Ledoux criterion formulated like so

$$\nabla_{\rm rad} > \nabla_{\rm ad} + (\varphi/\delta)\nabla_\mu, \tag{3}$$

but instead uses a form for a generalized EOS as described in appendix A of Heger et al. (2005), and also includes thermohaline convection (e.g. Woosley et al. 2004). A detailed description of the mixing physics, including the semiconvective diffusion coefficient and the treatment of overshooting, can be found in Sukhbold & Woosley (2014).

2.2.7 Initial models and treatment of the pre-main sequence

In KEPLER, the initial model is set up as a polytrope with index $n = 3$ and central density of $\rho = 0.1\,{\rm g\,cm^{-3}}$. The APPROX-19 network accounts for ^{3}He and follows its burning in the pre-MS phase just as is does during the rest of the evolution; other light isotopes such as deuterium of lithium are not considered explicitly. The pre-MS in GENEC is not considered in this work. The structure is converged from an approximative ZAMS structure, homogeneous in chemical composition. It requires a few tens of time steps to converge towards a stabilized ZAMS structure that is considered to be reached once the centre of the star is depleted by 0.003 of its initial H content (in mass fraction). The initial models in MESA are $n = 1.5$ polytropes with central temperatures of 9×10^6 K. The EOS and the mixing length theory routines are called iteratively by the Newton–Raphson solver to converge the total mass of the star, with the central density as the independent variable (see Paxton et al. 2011). The evolution loop including the complete (user specified) reaction network is then begun starting from the initial model.

2.3 Nucleosynthesis post-processing tool (MPPNP)

We use the NuGrid[3] multizone post-processing nucleosynthesis tool MPPNP (Pignatari et al. 2013b) to calculate the evolution of the composition in all of the stellar models in our comparison. From every time step calculated by the stellar evolution codes, MPPNP reads the thermodynamic trajectories (T and ρ) for the entire star and with a reaction network of 1088 nuclear species performs a fully implicit Newton–Raphson calculation to evolve the composition. This nuclear-burning step is then followed by a mixing step that solves the diffusion equation using diffusion coefficients from the stellar evolution calculations. For more details of the NuGrid post-processing tool MPPNP and the reaction rate compilations that we use, we refer the reader to Bennett et al. (2012) and Pignatari et al. (2013a). We used the same key energy-producing reaction rates as are used in the MESA and GENEC stellar evolution calculations to ensure consistency where possible.

3 STRUCTURAL EVOLUTION

In this section, we describe differences in the stellar models arising from the different physics assumptions and numerical implementation of the codes, which will later be connected to differences in the nucleosynthesis. We separate the description of the hydrogen- and helium-burning evolution in this section into two parts, concerning the interior (Section 3.1) and the surface (Section 3.2).

---

[3] www.nugridstars.org

3.1 Evolution of convective hydrogen- and helium-burning cores

3.1.1 Core hydrogen burning

During the MS evolution of a massive star, fusion of hydrogen into helium in the convective core results in a reduced opacity and increased mean molecular weight, μ. The increase in μ leads to an increase in luminosity ($L \propto \mu^4$). The outer layers expand, exerting less weight on the core, which also experiences a decrease in pressure. The reduction in opacity and pressure dominate over the increase in luminosity during the MS and because $\nabla_{\rm rad} \propto \kappa L_r P$, the radiative temperature gradient decreases. The adiabatic temperature gradient on the other hand, remains more or less unchanged. As a result, the material at the edge of the core becomes convectively stable and therefore the mass of the convective core decreases during the MS lifetime of the star. As the convective core recedes in mass, it leaves above it a (convectively stable) region of radially decreasing mean molecular weight, i.e. with $\nabla_\mu \equiv \partial \ln \mu / \partial \ln P > 0$.

The time evolution of the mass of the convective core is shown in Fig. 1 for the three masses we consider, computed with the three stellar evolution codes (MESA, black curve; GENEC, blue curve; KEPLER, silver curve). The location of the boundary of the convective core at the ZAMS is not dependent on the choice of convective stability criterion (Schwarzschild or Ledoux), since the chemical composition of the star is initially homogeneous. This is confirmed by comparing the KEPLER (Ledoux) and MESA (Schwarzschild) convective core masses at the ZAMS (Fig. 1). There are, however, differences between the MESA/KEPLER models and the GENEC models already at the ZAMS due to the assumption of core overshooting. Since GENEC assumes instantaneous, penetrative overshooting, the overshoot region is always an extension of the convective core that is effective immediately and thus its convective cores are already more massive than in the other two codes at the ZAMS.

As described earlier, in KEPLER convective stability is defined by the Ledoux criterion and semiconvection is considered. Although the semiconvection is comparably fast (Weaver et al. 1978; Sukhbold & Woosley 2014), it is still much slower than the mixing caused by either convection or overshooting. Thus in the GENEC models, which use the Schwarzschild criterion with a penetrative overshooting of $0.2\,H_P$, the resulting convective cores are larger than in those calculated with KEPLER for the entire duration of the MS. The gradient $\mathrm{d}M_{\rm core}/\mathrm{d}t$ is steepest in KEPLER because the gradient of chemical composition ∇_μ provides extra stability against convection in the region above the core that was previously part of the convective core. In the MESA models, the Schwarzschild criterion is used to define convective stability, as in GENEC, but overshooting is treated diffusively with a diffusion coefficient that decays exponentially into the radiative zone. Not only does this result in different extents of mixing in the two codes, but also in different time-scales of the extra mixing. In GENEC the convective region is assumed to be instantaneously mixed during core H and He burning while MESA's diffusive approximation accounts for the time dependency of mixing. $|\mathrm{d}M_{\rm core}/\mathrm{d}t|$ during the MS is thus smallest (shallowest curve) for MESA because the time-dependent diffusive treatment of overshooting mixes fresh fuel into the core more slowly than the instantaneous mixing in GENEC. Although the convective core mass at the ZAMS is the same for the KEPLER and MESA models, the diffusive treatment of overshoot mixing in MESA always results in a larger convective core mass at the terminal-age main-sequence (TAMS) for the assumed value of $f_{\rm CBM} = 0.022$ (see equation 2).
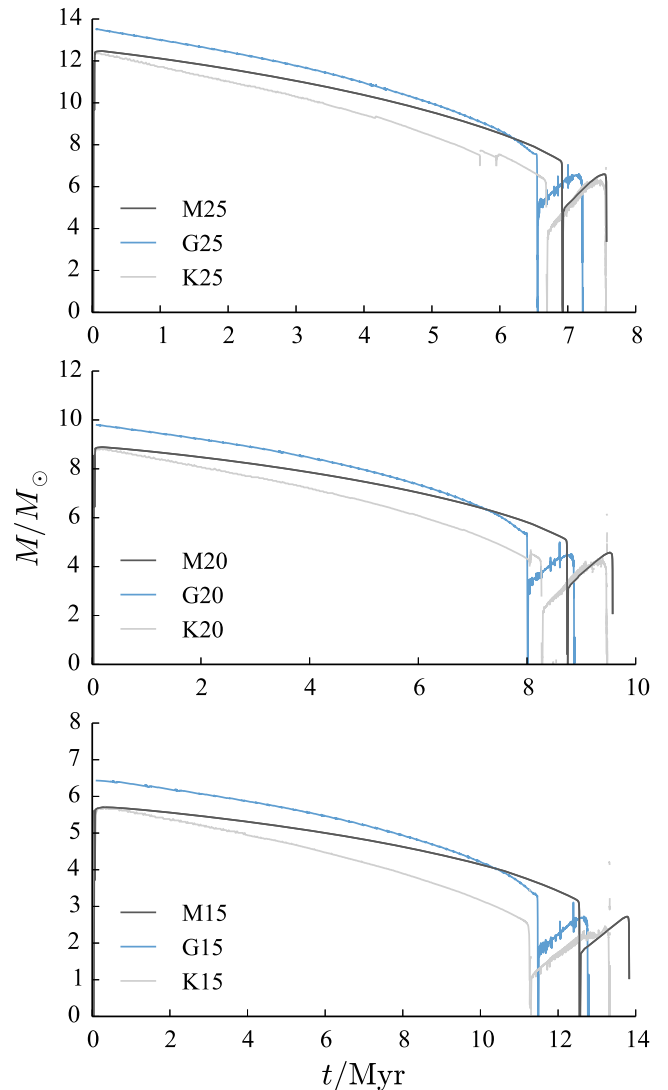

Figure 1. Convective core masses as a function of stellar age (Myr) during the core hydrogen- and helium-burning phases for the $15\,\mathrm{M_\odot}$ (bottom panel), $20\,\mathrm{M_\odot}$ (middle panel) and $25\,\mathrm{M_\odot}$ (top panel) models.

As a star evolves along the MS, its mean molecular weight μ increases, as does its luminosity, L. For a given initial mass, the luminosities calculated by the KEPLER and GENEC codes at the ZAMS agree very well (Fig. 2). The ZAMS luminosities of the MESA models are slightly higher because the convective core is initially slightly more compact (smaller radius). This small difference is likely due to the different treatment of the pre-MS phase, which is described in Section 2.2.7 for the three codes.

As the models evolve along the MS, the GENEC and MESA models have very similar luminosities for a given initial stellar mass. KEPLER, on the other hand, exhibits the lowest luminosities during the MS after the ZAMS because of its smaller cores. The MS lifetime is determined by the luminosity and the amount of fuel available. The hydrogen-burning lifetimes in the GENEC and KEPLER models agree reasonably well, with MESA always lasting longer on the MS. This can be attributed to the fact that although GENEC has higher luminosities than KEPLER because of its larger convective cores, and so would burn its fuel quicker, it also has more fuel available. MESA, on the other hand, exhibits slower growth in luminosity during the
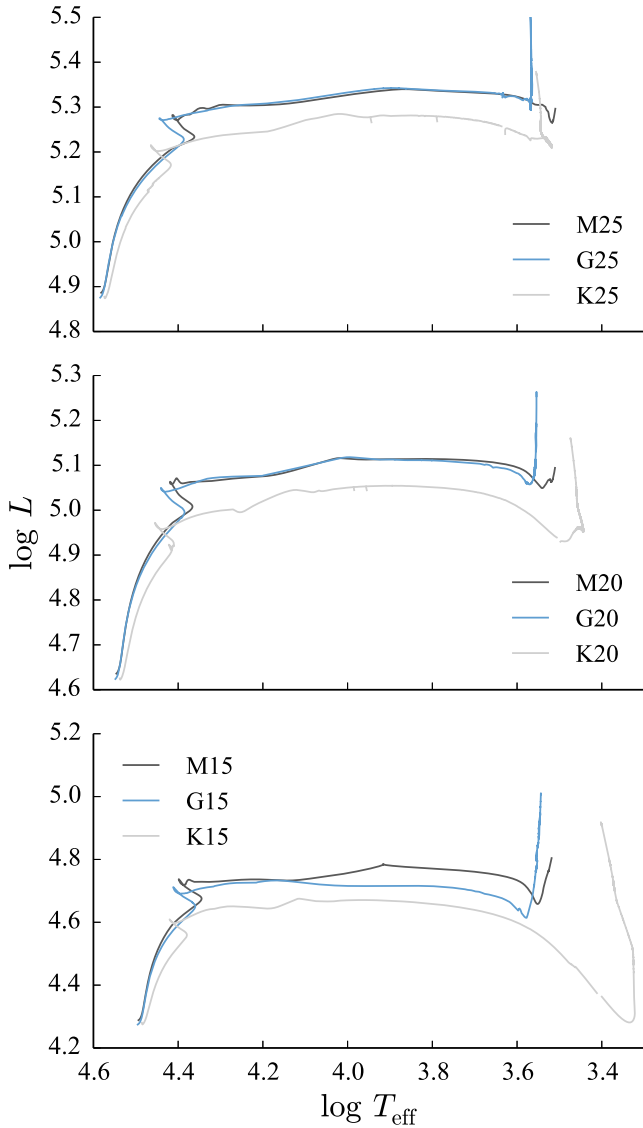
Figure 2. Evolution of the models in the HRD. Top, middle and bottom panels show 25, 20 and 15 $M_\odot$ models, respectively.

Table 3. Nuclear-burning lifetimes of all the stellar models with average values and standard deviations.

Model	$\tau_H/10^6$ yr	$\tau_{He}/10^5$ yr
G15	11.4	13.0
K15	11.2	20.5
M15	12.5	12.9
Average	11.7 ± 0.545 (5 per cent)	15.5 ± 3.58 (23 per cent)
G20	7.97	8.67
K20	8.24	12.0
M20	8.68	8.44
Average	8.30 ± 0.294 (4 per cent)	9.71 ± 1.64 (17 per cent)
G25	6.52	6.74
K25	6.66	8.77
M25	6.88	6.58
Average	6.69 ± 0.146 (2 per cent)	7.36 ± 0.996 (14 per cent)

reaction rate has a second-order dependence on the density while the $^{12}C(\alpha, \gamma)^{16}O$ reaction has only a first-order dependence. It is the latter reaction that dominates the later part of helium burning. It is the ingestion of fresh helium into the late helium burning that significantly reduces the central carbon-to-oxygen ratio at the end of central helium burning and thereby has major impact on carbon burning and beyond. The C/O ratio in the core at the end of the helium-burning phase is discussed in more detail in Section 3.1.3.

In their longer helium-burning lifetimes, the convective core masses in the KEPLER models have longer to grow and eventually become very similar to those in GENEC by the point of central helium depletion (Fig. 1). In KEPLER the semiconvection is fast enough to allow growth of the convective helium core whereas in plain Ledoux convection often a split of the convective helium burning may be found. Note also that the semiconvection during hydrogen burning in KEPLER can leave behind an extended region enriched in helium, however, the first dredge-up may remove the outer part of this enriched region. An extended region enhanced in helium may allow the hydrogen shell to grow faster than in other cases. The MESA models develop the largest convective helium cores for all of the three initial masses that we have considered, even though the MESA models have the shortest helium-burning lifetimes (very closely followed by GENEC). This can be attributed to the more massive hydrogen convective core at the TAMS in the MESA models. The mass of the hydrogen and helium convective cores has important implications for both the later evolutionary phases and the structure at the pre-supernova stage, since they are strongly coupled to the mass of the helium and CO cores (M_α and M_{CO}, respectively) at the pre-supernova stage. Thus, the relationship between the different codes for a given core mass (M_α, M_{CO}, etc.) at the pre-supernova stage is the same as is discussed above (see Table 4), with the codes generally agreeing to within a few per cent.

3.1.3 C/O ratio at the end of core helium burning

In addition to the CO core mass, the carbon-burning evolution is very sensitive to the C/O ratio at the end of the helium-burning phase. The ratio of carbon to oxygen in the centre of all the models at the time when the helium abundance first falls below $X_C(^4He) = 10^{-5}$ is shown in Table 5. A lower C/O ratio is indicative of higher temperatures and lower densities during core helium burning – these conditions favour $^{12}C(\alpha,\gamma)^{16}O$ over the 3α reaction (Woosley et al. 2002). As a result, the C/O ratio at the end of core helium burning is lower for larger initial stellar mass. Another important

MS than GENEC due to its diffusive treatment of overshooting. Fuel is constantly being mixed into the hydrogen-burning core in the MESA models and as a result they show the longest MS lifetimes of the three codes (see Table 3; again, these values are for $f_{CBM} = 0.022$).

3.1.2 Core helium burning

As described above and shown in Fig. 1, the KEPLER models have consistently less massive convective cores at the TAMS than the models calculated with the other two codes, which means that they are less luminous throughout the core helium-burning phase and thus have consistently longer helium-burning lifetimes (see Table 3). The convective core of a massive star grows in mass during the helium-burning lifetime (see Fig. 1). This is because the mass of the helium (hydrogen-free) core is also growing in mass due to shell hydrogen burning. The core luminosity therefore increases and more helium-rich material becomes convectively unstable. Two other factors are the increase of opacity due to the burning of helium to carbon and oxygen and the density–sensitivity of the 3α reaction rate. The 3α

Table 4. Total stellar mass (M_{tot}) and masses of the helium (M_α) and carbon–oxygen (M_{CO}) cores at the end of core He burning.
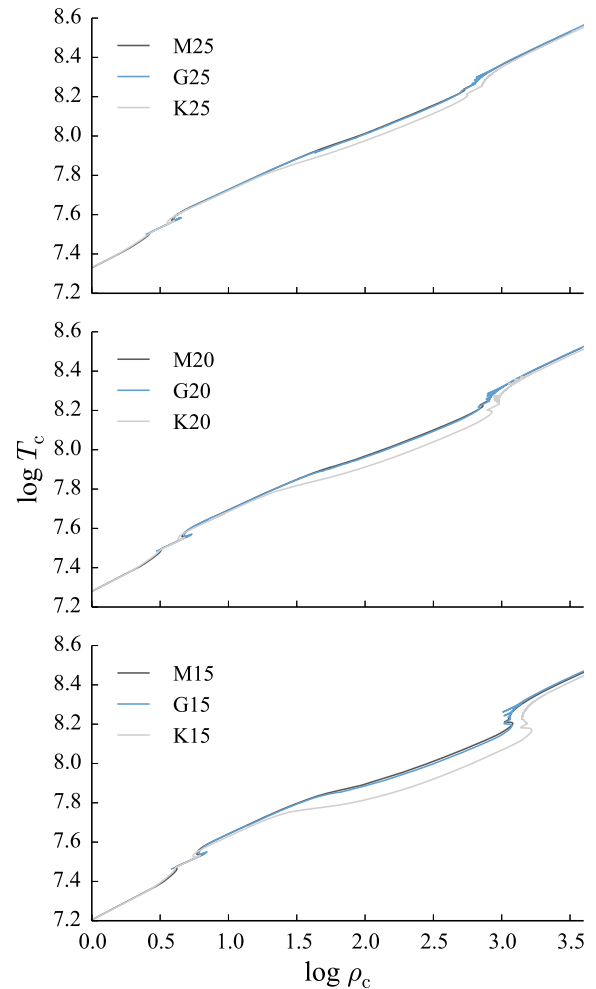
Model	$M_{tot}/M_\odot$	$M_\alpha/M_\odot$	$M_{CO}/M_\odot$
G15	12.13	4.79	2.86
K15	10.77	3.94	2.64
M15	12.15	4.76	2.99
Average	11.69 ± 0.65	4.40 ± 0.39	2.83 ± 0.15
	(6 per cent)	(9 per cent)	(5 per cent)
G20	13.97	6.83	4.54
K20	13.11	5.99	4.38
M20	15.40	6.77	4.65
Average	14.16 ± 0.944	6.53 ± 0.383	4.52 ± 0.112
	(7 per cent)	(6 per cent)	(2 per cent)
G25	13.74	9.19	6.48
K25	12.34	8.14	6.28
M25	12.82	9.13	6.82
Average	12.97 ± 0.580	8.82 ± 0.484	6.53 ± 0.220
	(4 per cent)	(5 per cent)	(3 per cent)

Table 5. C/O ratios at the end of core helium burning for all the stellar models, both from the networks that were used to compute stellar structure (upper half) and from MPPNP (lower half).

Code	$15\,M_\odot$	$20\,M_\odot$	$25\,M_\odot$
	Stellar structure networks		
GENEC	0.499	0.424	0.372
KEPLER	0.288	0.261	0.235
MESA	0.433	0.391	0.360
	Post-processing network		
GENEC	0.509	0.436	0.384
KEPLER	0.347	0.321	0.293
MESA	0.410	0.408	0.318

Figure 3. Evolution of the central temperature and density during the core hydrogen- and helium-burning phases.

factor is the treatment of convective boundary mixing. The diffusive treatment of the extra mixing at the edge of the helium core in the KEPLER and MESA models favours a lower C/O ratio. This is because additional α particles can be mixed into the convective core for the duration of the burning stage. In particular, the end of core helium burning is especially sensitive. A large proportion of the α particles newly introduced into the core at this time will react with carbon to produce oxygen, rather than reacting with other αs to produce carbon. This can be attributed to the sensitivity of the latter reaction to the cube of the α abundance. The behaviour of the convective helium core as it approaches helium exhaustion has been the subject of much discussion in the past. In particular, the presence of a 'core breathing' phenomenon (see e.g. Castellani et al. 1985). The build-up of ^{12}C and more critically ^{16}O increases the opacity in the core and hence the radiative temperature gradient also increases. In such a region at the edge of the core there is also a steep gradient of the mean molecular weight μ. The convectively stabilizing effect of the μ gradient is overlooked by codes that adopt the Schwarzschild criterion for convection, but not by those that adopt the Ledoux criterion and consider the effects of semiconvective mixing. The convective core must thus grow to some extent in mass and thereby engulf fresh ^{4}He. The central abundances of ^{4}He, ^{12}C and ^{16}O are dramatically affected during such a 'breathing pulse'.

The decreasing trend of C/O ratio with initial mass is exhibited by the models from all three codes. This is true for both the inline

nuclear reaction networks and our full network calculation in post-processing mode (Table 5). MESA models achieve lower C/O than GENEC models for a given initial mass because of their slightly more massive cores and diffusive overshooting (see discussion above). Another interesting factor that we had not initially expected to affect the C/O ratio is the ^{22}Ne(α, n)^{25}Mg reaction rate. The ^{22}Ne competes via this reaction with ^{12}C to capture the α particles. It has in fact a large enough effect that the C/O ratio will be sensitive to the ^{22}Ne(α, n)^{25}Mg reaction rate. Of particular note is a result that in the M20 model excluding the ^{22}Ne(α, n) and ^{22}Ne(α, γ) reactions results in a C/O ratio of 0.382 as opposed to 0.395 when the reactions are included. This ratio is important for energy generation and the stellar structure during the post helium core burning evolution. Thus, ^{22}Ne should be included in even small nuclear reaction networks that are designed to calculate only the energy generation inside the star. The KEPLER models have the lowest C/O ratio for a given mass out of the three codes. This is orthogonal to the statement made earlier with regards to core mass, temperature, density and the C/O ratio. It is clear from the central temperature–density evolution (Fig. 3) that helium burns at lower temperature and higher density in the KEPLER models than in the models from the other two codes. Other influencing factors are thus at play in the KEPLER models. First, the 3α and ^{12}C(α, γ)^{16}O reaction rates are different in the KEPLER models (see Section 2.2). Secondly, neither ^{22}Ne nor ^{25}Mg is

included explicitly in the inline nuclear reaction network of KEPLER. We argue that this could compromise the accuracy of the network by not explicitly following the competition between ^{22}Ne and ^{12}C to capture the α particles that we described above. These two factors will influence the C/O ratio of the inline network of KEPLER, however, they should have no bearing on the full network calculation that is done in post-processing mode. Nevertheless, we do indeed find that the KEPLER models exhibit consistently the lowest C/O ratios even in our post-processing calculations. This is because the core helium-burning lifetimes in the KEPLER models are the longest. For example, Table 3 shows that K15 burns helium in the core for about 60 per cent longer than M15. Artificially reducing the helium-burning lifetime in the K15 model during the post-processing stage indeed affects the C/O ratio. When the helium-burning lifetime of K15 is set to be the same as in M15, C/O = 0.468, as opposed to 0.347 for the (longer) original lifetime. This is still a lower value than in G15, despite G15 having the higher temperature and lower density that favour a lower C/O. The sensitivity of the C/O ratio to the implementation of overshoot mixing (penetrative/diffusive) is highlighted by this simple test.

3.2 Surface properties and HRD

3.2.1 Evolution in the HRD

At a given metallicity and initial mass, opacities and nuclear reaction rates being the same, the evolution in the Hertzsprung–Russell diagram (HRD) during the MS is mostly determined by the evolution of the central convective core.[4] We have already discussed the relationship between convective core mass and luminosity in the section above for the MS. For the reasons explained there concerning the convective core, the KEPLER models exhibit a narrower width of the MS and a lower turn-off luminosity (Fig. 2).

The trajectory of a stellar model in the HRD after the MS turn-off is determined by a complex interplay between the helium core, the hydrogen-burning shell and the opacity of the envelope. In general, as the core contracts the envelope will expand – a mirroring effect. During the core helium-burning evolution the structure is more complicated than during the MS. This is because there is a hydrogen-burning shell between the core and the envelope. The hydrogen-burning shell in fact provides a large fraction of the stellar luminosity during core helium burning. Fig. 4 shows effective temperature as a function of central helium abundance for the models.

The KEPLER models of all three initial masses ignite helium burning distinctly in the Hertzsprung gap. This only occurs in the 20 M$_\odot$ GENEC model while for MESA both the 20 and 25 M$_\odot$ models undergo a blue helium ignition. GENEC still displays the reddest helium ignition of the 20 M$_\odot$ models. In the 20 M$_\odot$ MESA model, shell hydrogen burning is initially very strong and a thick convection zone in the hydrogen shell develops. This provides a substantial fraction of the star's luminosity and therefore the core requires a slower rate of contraction in order to maintain hydrostatic equilibrium than if such a strong hydrogen shell were not present. The envelope expands less by the 'mirror effect' and as a result the star ignites helium before becoming a red supergiant. Out of all the KEPLER models, the 20 M$_\odot$ model also develops the strongest convective hydrogen shell. At the TAMS, the KEPLER models have lower helium core masses than the
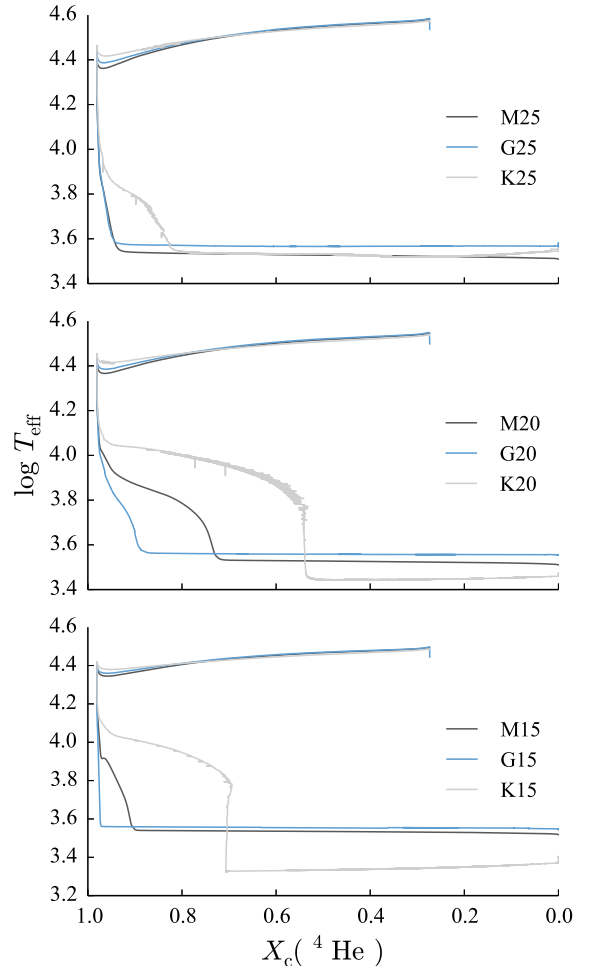
---

[4] In the mass range considered in this paper, the mass loss during the MS is weak enough not to influence significantly the tracks in the HRD. This is not the case for higher mass models with $M > 25$ M$_\odot$.


Figure 4. Effective temperature as a function of central ^{4}He abundance for the 15 M$_\odot$ (bottom panel), 20 M$_\odot$ (middle panel) and 25 M$_\odot$ (top panel) models. In these diagrams, the evolution proceeds from the top right-hand corner to the top left-hand corner during the MS and from the left to bottom right-hand corner during He burning.

other codes – the core contains a lower fraction of the total mass of the star, and thus the mirror effect is less, favouring a bluer helium-burning ignition than in the other codes. This is a consequence of the use of the Ledoux criterion. On the other hand, the region above the core is more enriched in helium allowing this more vigorous hydrogen shell burning. Georgy et al. (2013) have shown that for rotating massive star models, a hydrogen profile at the end of the MS that drops steeply at the edge of the helium core favours the blue ignition of helium. In accord, a shallow hydrogen profile above the helium core at the end of the MS favours a quicker evolution to the red supergiant (RSG) phase. This is because with an extended hydrogen profile the hydrogen shell will migrate outward in mass more rapidly and thus the core mass will increase faster, leading to its contraction and hence, to the expansion of the envelope. These differences arose in models that had very similar structures as the TAMS, and thus the work of Georgy et al. (2013) does not rule out other factors influencing the star's evolution towards becoming a red supergiant. The variation in the evolutionary tracks of the models in Fig. 4 is also due to the differences in the duration of the convective H-shell from model to model. The models spending the largest fraction of their helium-burning lifetimes in the bluer, hotter side of the HRD are those with the longest convective H-shell
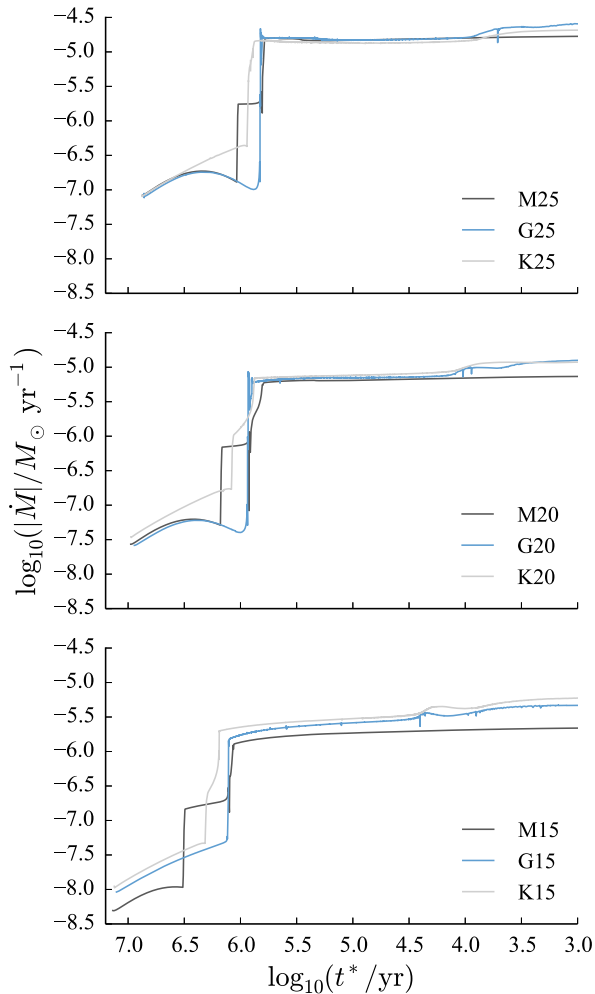
Figure 5. Mass-loss rates (in $M_\odot$ yr^{-1}) as a function of $\log_{10}(t^*/\mathrm{yr})$, where t^* is the time left until core collapse.

duration. The H-shell efficiency is for the most part set by the total stellar luminosity. Thus, the lowest luminosity models will be able to sustain a convective H-shell for longer. The total stellar luminosity at this time is a product of the core mass, which is in turn a product of the extent of convective H-burning core during the MS. The KEPLER models have the smallest convective hydrogen-burning cores (Fig. 1 and Table 4) and thus spend the largest fraction of their helium-burning lifetimes in the bluer, hotter side of the HRD.

3.2.2 Mass loss

The mass-loss rates of our models are shown as a function of time until core collapse in Fig. 5. As we have discussed in Section 2.2.4, the rate of mass loss from the stellar surface depends strongly on the position of the star in the HRD (i.e. its effective temperature and luminosity). Mass loss is generally stronger for higher luminosity and lower effective temperature, meaning that 15–25 $M_\odot$ stars experience modest mass loss during the MS, strong mass loss during the RSG phase and an intermediate rate of mass loss on the blue supergiant (BSG) phase.

Despite mass loss being modest during the MS, we still find significant discrepancies between the codes. The general shapes of the mass-loss curves as a function of time (shown in Fig. 5) during the MS fall into two categories. Those models assuming the mass-

loss rates of Vink et al. (2001) – the 20 and 25 $M_\odot$ GENEC models and all of the MESA models – experience a diminishing mass-loss rate before the end of the MS. This is due to the second-order polynomial dependence on the effective temperature of the Vink et al. (2001) mass-loss prescription. The KEPLER models (Nieuwenhuijzen & de Jager 1990 mass-loss rate) and the 15 $M_\odot$ GENEC model (de Jager et al. 1988 mass-loss rate) do not experience a reduction in mass loss towards the end of the MS. The sharp increase in the mass-loss rate of the MESA models (by about a factor of 10) during the MS is caused by the transition from the hot side to the cool side of the bistability limit (Vink et al. 2001, and references therein). The transition across the bistability limit is not seen in the (20 and 25 $M_\odot$) GENEC models that use the same mass-loss rates (Fig. 5), even though their evolution in the HRD (in particular, their effective temperatures) is very similar to the MESA models (Fig. 2). This is a result of the way in which the bistability limit is used in the two codes. In GENEC, the bistability temperature limit $T_{\mathrm{eff}}^{\mathrm{jump}}$ is calculated using equations (14) and (15) of Vink et al. (2001), and the mass-loss rate is calculated based on whether the effective temperature is hotter or cooler than $T_{\mathrm{eff}}^{\mathrm{jump}}$. In MESA, the transition in mass-loss rate from the hot side to the cool side of the bistability limit is smoothed for effective temperatures in the range $-100 < T_{\mathrm{eff}} - T_{\mathrm{eff}}^{\mathrm{jump}} < 100$ K. The resulting mass-loss rate for a star with effective temperature in this range is a weighted average of the hot- and cool-side rates.

The total stellar mass is relatively fixed following central helium depletion because of the rapidity of the remaining evolutionary phases compared with the mass-loss rate. Two striking features are that first, the total mass of K15 is significantly lower than in G15 or M15, which agree very well (Table 4). This is due to higher mass-loss rates during the RSG phase as a result of the significantly lower effective temperature. The lower effective temperature in the KEPLER model is explained by the different integration method for the envelope, which yields effective temperatures that are too low. This also affects the effective temperature of the 20 $M_\odot$ model to a smaller extent. Secondly, the amount of mass retained in the envelope in M20 is significantly higher than in G20 or K20. This is due to the combined effect of two influencing factors. First, the model spends some of its helium-burning lifetime as a blue supergiant with higher effective temperature and lower luminosity. Secondly, the total helium-burning lifetime of M20 is shorter than in G20 or K20 and thus less mass is lost. Lower T_{eff} and higher L can be seen to result in stronger mass loss (the increase in mass loss during the RSG stage) for example in the 15 $M_\odot$ models at $\log_{10}(t^*/\mathrm{yr}) \approx 6$ in the lower panel of Fig. 5.

4 NUCLEOSYNTHESIS UP TO END OF CORE HELIUM BURNING

After discussing the differences in the structure of the models calculated with the three stellar evolution codes, in this section, we discuss the nucleosynthesis results obtained until the end of core helium burning. The nucleosynthesis was calculated using the same post-processing code for all models, adopting the same nuclear reaction network and rates (see Section 2.3). In this study, we focus on the evolution of the surface composition (Section 4.1) and the weak s-process production during core helium burning (Section 4.2).

4.1 Envelope and surface composition

Following the MS, the envelopes of massive stars become convective, reaching down and dredging up material that has been processed by the hydrogen-burning core and shell. This dredge-up
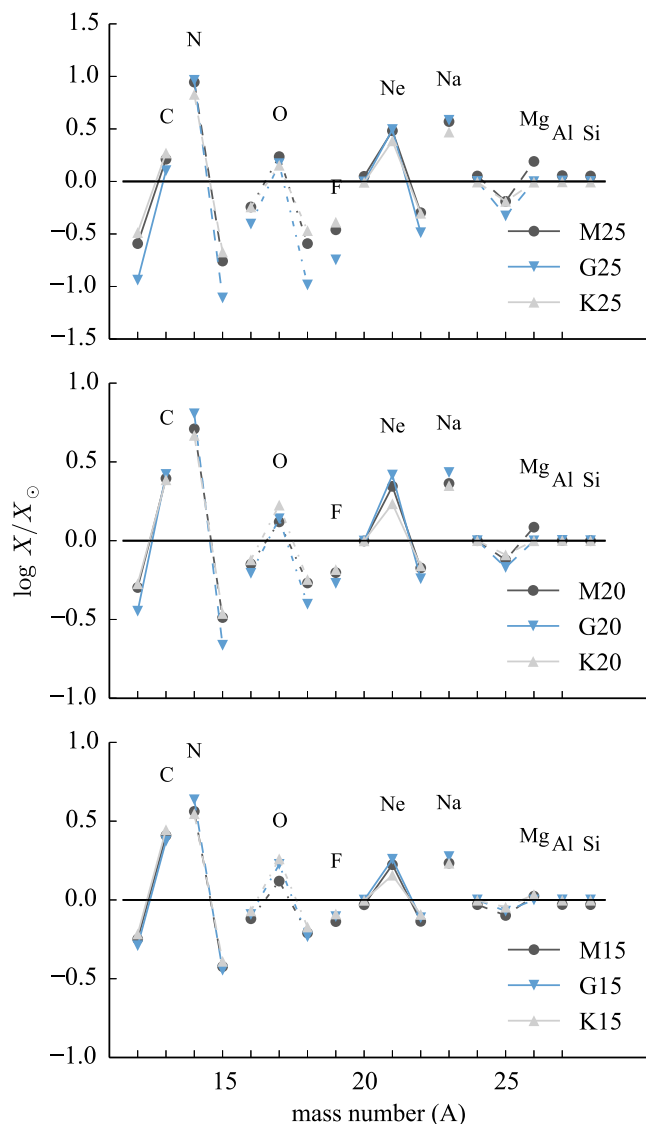
Figure 6. Surface overabundances ($X_i/X_\odot$) at the end of the core helium-burning phase.

4.2 Nucleosynthesis up to the end of core He burning

During the convective core helium burning, the important reactions competing for the economy of the α particles are the $3\alpha \rightarrow {}^{12}$C, ^{12}C($\alpha$, γ)^{16}O and the ^{22}Ne+α reactions, although the latter two from this list is only activated at the end of core helium burning (e.g. Raiteri et al. 1991). The growth of the convective helium core and the treatment of mixing across its convective boundary are critical factors in determining how much fresh helium is introduced into the core and at what rate. Introducing fresh helium into the convective core towards the end of the helium-burning phase when the helium abundance is becoming low is of particular importance. In this condition, the 3α reaction is less of a competitor for the other two reactions in consuming the freshly introduced helium and two things happen: the C/O ratio decreases (see Section 3.1 and Table 5) and the neutron exposure (or the total amount of neutrons made by the ^{22}Ne(α, n)^{25}Mg reaction) increases.

As described in Section 3.1, the convective core grows in mass over the duration of the helium-burning phase because of the growth of the helium core due to hydrogen shell burning and the increased opacity due to the conversion of helium into carbon and oxygen. The penetrative overshooting in GENEC introduces new helium-rich composition into the convective helium-burning core when it first develops, after which the composition is chemically homogenized by convection and uniformly depleted. The introduction of fresh, helium-rich material into the convective core can thus be considered only a result of the growth of the extent of the convective core and not the overshooting. In MESA on the other hand, fresh α particles are continuously mixed into the convective core from the radiative layers above. This is because of the diffusive treatment of convective boundary mixing in MESA and occurs even when the abundance of helium in the core is low, i.e. towards the end of the core helium-burning phase. Something similar occurs in the KEPLER models because semiconvection above the convective core is treated as a diffusive process. Also affecting the size of the convective core towards the end of core helium burning is the increase of the opacity due to the rising amounts of C and O. The radiative gradient (in particular, at the edge of the convective core) will increase as a result of this opacity increase (see Section 3.1 and the discussion of core breathing). In GENEC and MESA, which consider only the Schwarzschild criterion for convection, the convective core will engulf material from the overlying layers when this situation rises. In KEPLER on the other hand, which considers the Ledoux criterion and semiconvection, the stabilizing effect of the mean molecular weight gradient across the interface of the convective core is considered. The mixing is thus semiconvective rather than convective, meaning that it would operate on the longer, secular time-scale instead of the convective time-scale.

In Fig. 7 the s-process distributions in the helium-depleted core from all of the models are shown at the end of the core helium-burning phase. The models agree well with the GENEC models always slightly underproducing compared with the KEPLER and MESA models. All three codes however produce results in the weak s-process region within 25 per cent (Fig. 8). The differences are mildest for the 15 M$_\odot$ models, with the three codes providing overproduction factors in the weak s-process region that are consistent to within 20 per cent. Note that for all three initial masses, our results from different stellar evolution codes show variations well within the impact due to nuclear reaction rate uncertainties (Pignatari et al. 2010; West et al. 2013).

A comparison of the weak s-process distribution at the end of the He core was already provided by Kaeppeler et al. (1994), where
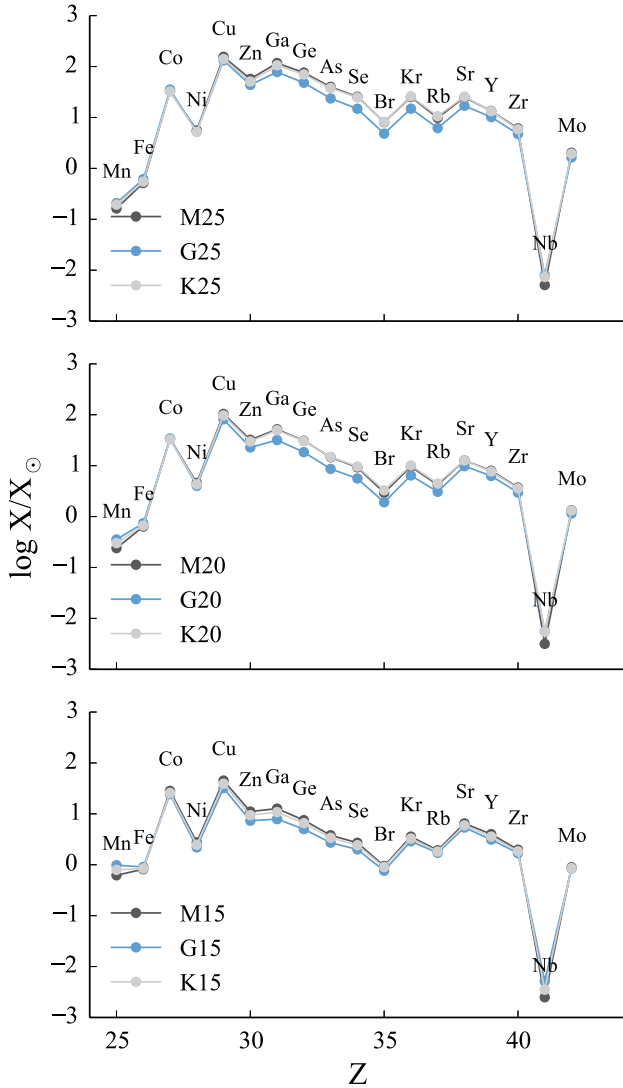
results in a CNO processing signature observed in the surface composition that persists until the pre-supernova stage. This signature includes a higher concentration of e.g. ^{13}C, ^{14}N and ^{23}Na and a lower abundance of e.g. ^{12}C, ^{15}N and ^{16}O (Fig. 6). This signature is stronger in more massive stars due to the more extended (in time) convective H-burning shell. Since it is mainly determined by nuclear reactions, this CNO processing signature is qualitatively extremely similar between the three codes, showing that the use of a different code has little impact in this context. In general, the H-burning signature on the surface is increasing with the initial mass of the star across the three codes. The small quantitative differences are the following. GENEC shows the strongest enrichment signature with the highest enrichment for ^{14}N and ^{23}Na. This is accompanied with a weaker enrichment in ^{13}C – which is a signature of incomplete CNO processing – and the strongest depletion in ^{12}C, ^{15}N and ^{16}O, whereas KEPLER (Ledoux with semiconvection) shows the smallest enrichment.

Figure 7. Overabundances (X/X_{ini}, where $X_{\mathrm{ini}} = X_\odot$) in the inner $1\,\mathrm{M}_\odot$ at the end of the core helium-burning phase.
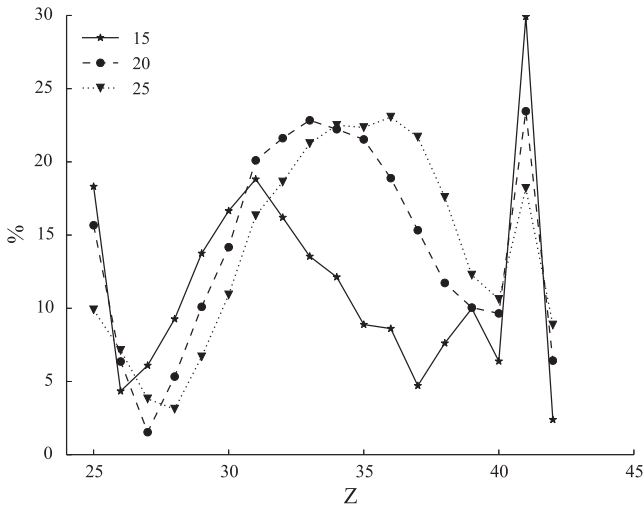

Figure 8. Standard deviations (as percentages) between the three stellar evolution codes (MESA, KEPLER and GENEC) for the elemental overproduction factors (X/X_{ini}, where $X_{\mathrm{ini}} = X_\odot$) in the helium core.

Table 6. ^{80}Kr overproduction factors at the end of core helium burning.

Code	$15\,\mathrm{M}_\odot$	$20\,\mathrm{M}_\odot$	$25\,\mathrm{M}_\odot$
GENEC	11.2	29.9	76.3
KEPLER	13.7	52.1	137.5
MESA	15.3	49.3	136.6
Max/min	1.37	1.74	1.80
Average	13.4 ± 1.7	43.8 ± 9.9	116.8 ± 28.6
	(13 per cent)	(23 per cent)	(24 per cent)

the results from the codes FRANEC and GÖTTINGEN were discussed for massive stars with a range of initial masses. In that work the differences were much larger than what we obtained here. The production factors of ^{80}Kr in the work by Kaeppeler et al. (1994) show a spread between factors of 3 (for the $30\,\mathrm{M}_\odot$ models) and 25 (for the $15\,\mathrm{M}_\odot$ models). In our models, the ^{80}Kr production factors agree within a factor of 2 for a given initial stellar mass (Table 6). The standard deviations between the three codes for each initial mass and element are shown in Fig. 8 for the elemental production factors in the helium core. Part of the reason for the spread found by Kaeppeler et al. (1994) is that while the codes were using the same ^{22}Ne + α rates, different nucleosynthesis networks were used for the simulations. Here we obtain a better consistency (within 25 per cent for the s-process region) for models with a similar range of stellar masses, giving a brighter view from the comparison.

In general, for different initial masses and codes Cu has the highest production efficiency by the weak s-process at the end of the He core (e.g. Pignatari et al. 2010). On the other hand, the production of heavier s-process elements like Ga and Ge depends on the initial mass of the star and on the code, i.e. on the amount of neutrons made by the ^{22}Ne$(\alpha, n)^{25}$Mg.

In Fig. 9 the evolution of the ^{4}He and ^{80}Kr abundances in the convective He-burning core is shown with respect to phase (where phase = 0 at helium ignition and 1 at helium depletion). ^{80}Kr is defined as an s-only isotope, but it also receives a relevant explosive contribution, from the classical p-process (e.g. Arnould & Goriely 2003), from neutrino-driven wind nucleosynthesis components (e.g. Fröhlich et al. 2006; Farouqi et al. 2010; Arcones & Montes 2011) and eventually from α-rich freeze-out ejecta (Woosley & Hoffman 1992). Its production in s-process conditions strongly depends on the branching in the neutron-capture path at ^{79}Se (Klay & Käppeler 1988). We focus in particular on ^{80}Kr in Fig. 9 because there are detailed results for this nucleus reported in the study by Kaeppeler et al. (1994) to which we will have compared the results of our calculations. The increase of ^{80}Kr starts during the last 10 per cent of the He-burning lifetime ($\log(1 - \mathrm{phase}) = -1$ in Fig. 9). Since ^{22}Ne is not fully consumed during the He core, ^{80}Kr increases until the reservoir of α-particles is exhausted. Furthermore, the amount of ^{80}Kr made increases with the initial mass of the star (note the different y-axis scales on the right-hand side of Fig. 9). This means that the s-process efficiency increases with the initial mass of the star because of the higher central temperatures and the more efficient ^{22}Ne$(\alpha, n)^{25}$Mg activation, as already discussed by Prantzos, Hashimoto & Nomoto (1990). This trend of increasing s-process efficiency with increasing initial stellar mass is also shown in Fig. 7. The evolution of the central temperature and ^{22}Ne abundance during the core helium-burning phase is shown in Fig. 10. The values of these two quantities at the end of the core helium-burning phase is given together with the abundance of ^{56}Fe in Table 7.
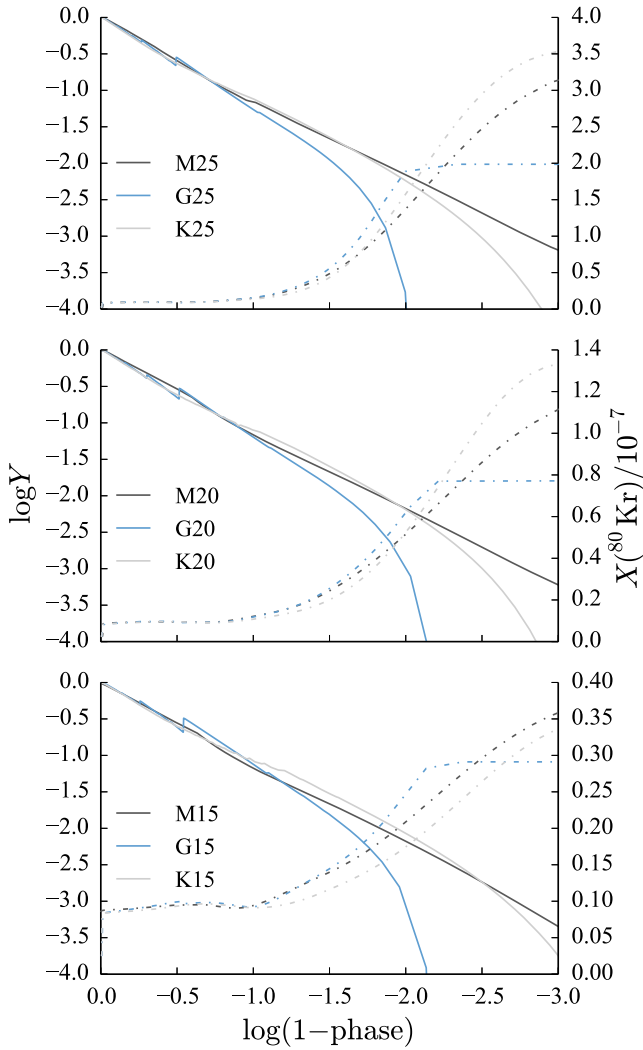
Figure 9. Central ^{4}He (solid lines) and ^{80}Kr (s-only; dot–dashed lines) abundances during the core helium-burning phase. The *x*-axis is log $(1 - \text{phase})$, where phase = 0 at helium ignition (left-hand side of the plot) and 1 at helium depletion (right-hand side of the plot).

Figure 10. Central ^{22}Ne abundances (dashed lines) and central temperatures (solid lines) during the core helium-burning phase.

Table 7. Central abundance (mass fraction) of ^{22}Ne and central temperature at the end of core helium burning.

Model	$X_C(^{22}\text{Ne})/10^{-2}$	$X_C(^{56}\text{Fe})/10^{-3}$	$T_C/10^8$ K
G15	1.506	0.704	3.23
K15	1.384	0.637	3.11
M15	1.329	0.588	3.11
G20	1.100	0.457	3.40
K20	0.940	0.409	3.28
M20	0.900	0.377	3.29
G25	0.768	0.331	3.55
K25	0.615	0.306	3.39
M25	0.544	0.272	3.36

The three codes that were used to produce these stellar models assumed different formulations for the treatment of convective boundary mixing (CBM) above the convective He core. These are penetrative overshooting (GENEC), fast semiconvection (KEPLER) and exponentially decaying diffusive overshooting (MESA). These formulations are described in more detail in Section 2.2.6. The impact of overshooting on the weak s-process was considered by e.g. Langer, Arcoragi & Arnould (1989) and Pumo et al. (2010), showing that in general the s-process production increase with the overshooting efficiency, due to the larger reservoir of ^{4}He. Fig. 9 shows that the s-process production (represented by ^{80}Kr) is drawn-out by continuous replenishment of α-particles in the KEPLER and MESA models due to their time-dependent, diffusive CBM treatments. Nevertheless, we show something new with these results compared to Langer et al. (1989): three alternative CBM formulations each with their own choice of parameters are providing consistent (overproduction of the weak s-process elements agreeing to within 25 per cent) s-process results at the end of the He core.
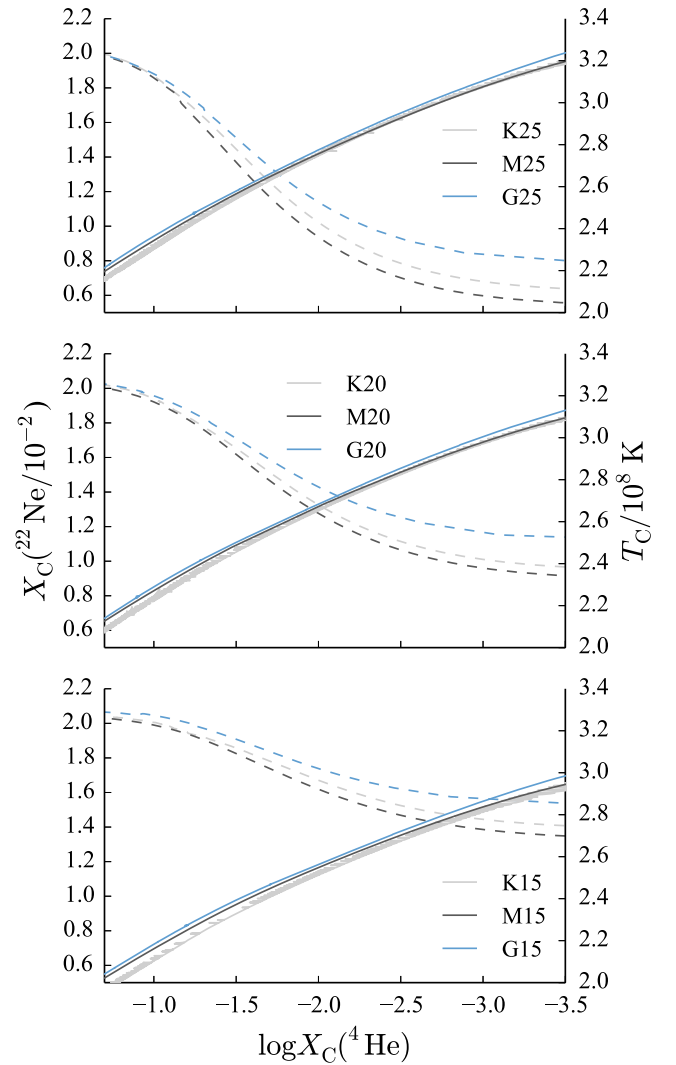
5 DISCUSSION AND CONCLUDING REMARKS

We have compared the structural evolution of stellar models from the GENEC, KEPLER and MESA stellar evolution codes. We chose models with initial masses 15, 20 and 25 M$_\odot$ at $Z = 0.02$, which is arguably the most studied massive star mass range. The models were analysed from the ZAMS to the end of the core helium-burning stage. We

have computed the full (1088 species) nucleosynthesis of all nine models in a post-processing mode using the NuGrid code MPPNP, in which a mixing (diffusion) step is performed after each network time step (i.e. the mix and burn operators are decoupled).

During the hydrogen- and helium-burning stages, the main differences in the structure of the models can be traced back to the different choices for the input physics. The key differences are the criterion for convective stability: Schwarzschild (GENEC and MESA) compared to Ledoux (KEPLER), the treatment of convective boundary mixing: penetrative overshooting (GENEC), exponentially decaying diffusion scheme (MESA) or semiconvection (KEPLER) as well as the mass-loss rate prescriptions and their implementation. The size of the convective core during the MS and the MS lifetime is mostly influenced by the treatment of convective boundary mixing or overshooting. The chemical composition of the core at helium depletion is very sensitive to the structural evolution during core helium burning. Particularly sensitive are the ratio of carbon to oxygen and the weak s-process component. The three codes show quite a large spread in the C/O ratio in the helium-depleted core owing to their different assumptions on convective boundary mixing and their different helium-burning lifetimes. Another factor is of course the rates used for the key nuclear reactions. Whereas the rates for the 3α and $^{12}C(\alpha, \gamma)^{16}O$ reactions are clearly important, the C/O ratio is also mildly sensitive to the choice of $^{22}Ne(\alpha, n)^{25}Mg$ and $^{22}Ne(\alpha, \gamma)^{26}Mg$ rates. Of course, the C/O ratio shows a more marked change when the α-capture channels of ^{22}Ne are omitted completely from the reaction network. This strongly suggests that ^{22}Ne should be included in even small networks whose aims are solely to accurately compute the energy generation to supplement the structural evolution of the stellar model.

The treatment of convective boundary mixing during the MS affects the hydrogen and helium profiles outside of the helium core. The location of the star in the HRD as the star is becoming a supergiant following the MS is very sensitive to these profiles (see Georgy et al. 2013). The KEPLER models spend less time as red supergiants than the MESA and GENEC models. This is because the duration of the convective hydrogen-burning shell is longest in the KEPLER models – a result of their smaller hydrogen-burning convective cores and hence lower luminosities. The MS lifetimes of the models from the three codes agree within 5 per cent or better for a given initial mass, while the helium-burning lifetimes show a much larger spread (up to 23 per cent in the 15 $M_\odot$ models). The core masses and total masses of the models at the end of core helium burning show spreads with standard deviations in the range 2–9 per cent. Particularly for the helium and CO core masses, the standard deviation is dominated by the smaller KEPLER cores (because of the choice of Ledoux criterion and semiconvection compared to Schwarzschild criterion and overshooting in the other two codes). That being said, the CO cores show less of a spread than the helium cores due to the longer helium-burning lifetimes in the KEPLER models. The spread is a little more even in the total stellar masses for the 20 and 25 $M_\odot$ models.

The main results concerning the differing nucleosynthesis in the models can be summarized as follows. The surface abundances show the characteristic signature of CNO enrichment, which is stronger for larger initial masses. This enrichment is linked to the physical extent and duration of the convective hydrogen-burning episode preceding the dredge-up and always shows the strongest signature in the GENEC models and the weakest in those of KEPLER. We compared the s-process results obtained at the end of the He core, with an approach similar to Kaeppeler et al. (1994) but using the same post-processing nuclear network for the three sets

of models. Compared to these earlier comparisons, we obtained much smaller departures between the results from different codes. Concerning the s-process elements between Fe and Sr, the largest differences are obtained for the overproduction factors of Ga (in the 15 $M_\odot$ models), As (in the 20 $M_\odot$ models) and Kr (in the 25 $M_\odot$ models), with standard deviations of 17, 23 and 23 per cent, respectively. The standard deviation of the elemental production factor of any element between Fe and Mo in the helium core is less than 30 per cent. These differences in the elemental overproduction factors are much smaller than the impact of the present nuclear physics uncertainties (e.g. Pignatari et al. 2010). Therefore, the three codes can be considered to yield consistent results. The discussion may be more complex for the single isotopes, where larger differences can be obtained, but overall we may conclude that the results are consistent. We anticipate that while the overproduction factors look consistent at the end of the helium core, the final production factors might be quite different due to e.g. the impact of different He core sizes, the s-process activation during the following convective carbon shells burning and the final core-collapse supernova modification of the ejected s-process abundances. The amount of weak s-process material for a given progenitor mass, however, may have implications for galactic chemical evolution studies (e.g. Brown & Woosley 2013).

The models presented in this paper show that the three stellar evolution codes yield consistent results, which is reassuring for the field. Differences in key properties of the models, like helium and CO core masses, are traced back to the treatment of convection (see also Sukhbold & Woosley 2014). The behaviour of the mixing processes in stars remains the uncertainty of primary concern in stellar modelling. Better constrained prescriptions are thus necessary to improve the predictive power of stellar evolution models. Multidimensional hydrodynamic simulations and asteroseismological observations will hopefully provide the necessary constraints to reduce the current uncertainties in the coming decade.

ACKNOWLEDGEMENTS

REFERENCES

Alexander D. R., Ferguson J. W., 1994, ApJ, 437, 879
Angulo C. et al., 1999, Nucl. Phys. A, 656, 3
Arcones A., Montes F., 2011, ApJ, 731, 5
Arnould M., Goriely S., 2003, Phys. Rep., 384, 1
Asplund M., Grevesse N., Sauval A. J., Scott P., 2009, ARA&A, 47, 481
Bennett M. E. et al., 2012, MNRAS, 420, 3047
Blinnikov S. I., Dunina-Barkovskaya N. V., Nadyozhin D. K., 1996, ApJS, 106, 171
Blinnikov S. I., Dunina-Barkovskaya N. V., Nadyozhin D. K., 1998, ApJS, 118, 603
Brott I. et al., 2011, A&A, 530, A115
Brown J. M., Woosley S. E., 2013, ApJ, 769, 99

Bruzual G., Charlot S., 2003, MNRAS, 344, 1000
Buchler J. R., Yueh W. R., 1976, ApJ, 210, 440
Buchmann L., 1996, ApJ, 468, L127
Buchmann L., 1997, ApJ, 479, L153
Canuto V., 1970, ApJ, 159, 641
Castellani V., Chieffi A., Tornambe A., Pulone L., 1985, ApJ, 296, 204
Caughlan G. R., Fowler W. A., 1988, At. Data Nucl. Data Tables, 40, 283
Cescutti G., Chiappini C., 2014, A&A, 565, A51
Chiappini C., Matteucci F., Gratton R., 1997, ApJ, 477, 765
Chin C.-W., 1965, ApJ, 142, 1481
Christy R. F., 1966, ApJ, 144, 108
Cooper G., 1973, Lawrence Livermore Laboratory, UCRL-7524
Couch S. M., Ott C. D., 2013, ApJ, 778, L7
Cyburt R. H. et al., 2010, ApJS, 189, 240
de Jager C., Nieuwenhuijzen H., van der Hucht K. A., 1988, A&AS, 72, 259
Eggenberger P., Meynet G., Maeder A., Hirschi R., Charbonnel C., Talon S., Ekström S., 2008, Ap&SS, 316, 43
Ekström S. et al., 2012, A&A, 537, A146
Eldridge J. J., Stanway E. R., 2009, MNRAS, 400, 1019
Eldridge J. J., Tout C. A., 2004, MNRAS, 353, 87
El Eid M. F., Meyer B. S., The L.-S., 2004, ApJ, 611, 452
Farouqi K., Kratz K.-L., Pfeiffer B., Rauscher T., Thielemann F.-K., Truran J. W., 2010, ApJ, 712, 1359
Ferguson J. W., Alexander D. R., Allard F., Barman T., Bodnarik J. G., Hauschildt P. H., Heffner-Wong A., Tamanai A., 2005, ApJ, 623, 585
Fraser M. et al., 2011, MNRAS, 417, 1417
Freytag B., Ludwig H.-G., Steffen M., 1996, A&A, 313, 497
Frischknecht U., Hirschi R., Thielemann F.-K., 2012, A&A, 538, L2
Fröhlich C., Hix W. R., Martínez-Pinedo G., Liebendörfer M., Thielemann F.-K., Bravo E., Langanke K., Zinner N. T., 2006, New Astron. Rev., 50, 496
Fynbo H. O. U. et al., 2005, Nature, 433, 136
Gasques L. R., Brown E. F., Chieffi A., Jiang C. L., Limongi M., Rolfs C., Wiescher M., Yakovlev D. G., 2007, Phys. Rev. C, 76, 035802
Georgy C. et al., 2013, A&A, 558, A103
Glebbeek E., Gaburov E., de Mink S. E., Pols O. R., Portegies Zwart S. F., 2009, A&A, 497, 255
Grevesse N., Noels A., 1993, in Prantzos N., Vangioni-Flam E., Casse M., eds, Origin and Evolution of the Elements. Cambridge Univ. Press, Cambridge, p. 15
Heger A., 1998, PhD thesis, Max-Planck-Institut für Astrophysik
Heger A., Woosley S. E., 2002, ApJ, 567, 532
Heger A., Langer N., Woosley S. E., 2000, ApJ, 528, 368
Heger A., Fryer C. L., Woosley S. E., Langer N., Hartmann D. H., 2003, ApJ, 591, 288
Heger A., Woosley S. E., Spruit H. C., 2005, ApJ, 626, 350
Henyey L. G., Forbes J. E., Gould N. L., 1964, ApJ, 139, 306
Herwig F., Bloecker T., Schoenberner D., El Eid M., 1997, A&A, 324, L81
Hubbard W. B., Lampe M., 1969, ApJS, 18, 297
Huebener W. F., Merts A. L., Magee N. H., Argo M. F., 1964, Los Alamos Laboratory Report, LA-6760-M
Iben I., Jr, 1975, ApJ, 196, 525
Iglesias C. A., Rogers F. J., 1996, ApJ, 464, 943
Imbriani G., Limongi M., Gialanella L., Terrasi F., Straniero O., Chieffi A., 2001, ApJ, 558, 903
Imbriani G. et al., 2004, A&A, 420, 625
Jaeger M., Kunz R., Mayer A., Hammer J. W., Staudt G., Kratz K. L., Pfeiffer B., 2001, Phys. Rev. Lett., 87, 202501
Jones S. et al., 2013, ApJ, 772, 150
Kaeppeler F. et al., 1994, ApJ, 437, 396

Kawata D., Gibson B. K., 2003, MNRAS, 340, 908
Klay N., Käppeler F., 1988, Phys. Rev. C, 38, 295
Kobayashi C., Karakas A. I., Umeda H., 2011, MNRAS, 414, 3231
Kunz R., Fey M., Jaeger M., Mayer A., Hammer J. W., Staudt G., Harissopulos S., Paradellis T., 2002, ApJ, 567, 643
Langer N., Arcoragi J.-P., Arnould M., 1989, A&A, 210, 187
Limongi M., Chieffi A., 2012, ApJS, 199, 38
Lodders K., 2003, ApJ, 591, 1220
Martins F., Palacios A., 2013, A&A, 560, A16
Maund J. R. et al., 2011, ApJ, 739, L37
Mukhamedzhanov A. M. et al., 2003, Phys. Rev. C, 67, 065804
Müller B., Janka H.-T., Marek A., 2012, ApJ, 756, 84
Nakamura K., Takiwaki T., Kuroda T., Kotake K., 2014, preprint (arXiv:e-prints)
Nieuwenhuijzen H., de Jager C., 1990, A&A, 231, 134
Nomoto K., 1984, ApJ, 277, 791
O'Connor E., Ott C. D., 2011, ApJ, 730, 70
Paxton B., Bildsten L., Dotter A., Herwig F., Lesaffre P., Timmes F., 2011, ApJS, 192, 3
Paxton B. et al., 2013, ApJS, 208, 4
Pignatari M., Gallino R., Heil M., Wiescher M., Käppeler F., Herwig F., Bisterzo S., 2010, ApJ, 710, 1557
Pignatari M. et al., 2013a, ApJ, 762, 31
Pignatari M. et al., 2013b, preprint (arXiv:e-prints)
Poelarends A. J. T., Herwig F., Langer N., Heger A., 2008, ApJ, 675, 614
Potekhin A. Y., Chabrier G., 2010, Contr. Plasma Phys., 50, 82
Prantzos N., Hashimoto M., Nomoto K., 1990, A&A, 234, 211
Pumo M. L., Contino G., Bonanno A., Zappalà R. A., 2010, A&A, 524, A45
Raiteri C. M., Busso M., Picchio G., Gallino R., Pulone L., 1991, ApJ, 367, 228
Raiteri C. M., Gallino R., Busso M., Neuberger D., Kaeppeler F., 1993, ApJ, 419, 207
Rauscher T., Thielemann F.-K., 2000, At. Data Nucl. Data Tables, 75, 1
Rauscher T., Heger A., Hoffman R. D., Woosley S. E., 2002, ApJ, 576, 323
Rogers F. J., Nayfonov A., 2002, ApJ, 576, 1064
Sampson D. H., 1959, ApJ, 129, 734
Saumon D., Chabrier G., van Horn H. M., 1995, ApJS, 99, 713
Schaller G., Schaerer D., Meynet G., Maeder A., 1992, A&AS, 96, 269
Smartt S. J., 2009, ARA&A, 47, 63
Spruit H. C., 2002, A&A, 381, 923
Sukhbold T., Woosley S., 2014, ApJ, 783, 10
The L.-S., El Eid M. F., Meyer B. S., 2007, ApJ, 655, 1058
Timmes F. X., Swesty F. D., 2000, ApJS, 126, 501
Tur C., Heger A., Austin S. M., 2007, ApJ, 671, 821
Tur C., Heger A., Austin S. M., 2009, ApJ, 702, 1068
Ugliano M., Janka H.-T., Marek A., Arcones A., 2012, ApJ, 757, 69
Vink J. S., de Koter A., Lamers H. J. G. L. M., 2001, A&A, 369, 574
Weaver T. A., Zimmerman G. B., Woosley S. E., 1978, ApJ, 225, 1021
West C., Heger A., Austin S. M., 2013, ApJ, 769, 2
Woosley S. E., Heger A., 2007, Phys. Rep., 442, 269
Woosley S. E., Hoffman R. D., 1992, ApJ, 395, 202
Woosley S., Heger A., Weaver T., 2002, Rev. Modern Phys., 74, 1015
Woosley S. E. et al., 2004, ApJS, 151, 75
Young P. A., Arnett D., 2005, ApJ, 618, 908
Yusof N. et al., 2013, MNRAS, 433, 1114

This paper has been typeset from a TeX/LaTeX file prepared by the author.